German Aerospace Center

Institute of Propulsion Technology

IB 225 – 2015 A 05

Anna Petersen

Basic turbine cascade flow experiments

Date: September 2015
Client: FP7-AAT-2010-RTD-1; No. 265455
Applied for: TFAST Project—Transition Location Effect on Shock Wave Boundary Layer Interaction

Head of the Institute:
Prof. Dr.-Ing. R. Mönig

Copying and communicating the contents of this document or any other information – even of sections – to third parties only with permission ☐ of the client, ☒ of DLR-Gö

DLR

Key words:

Straight turbine cascade, infrared, hot-film, loss coefficient, Schlieren technique, transition location, film cooling

Basic turbine cascade flow experiments

Abstract

DLR has to submit two deliverables in Workpackage 4. These contain several measurement techniques applied at a straight turbine cascade. The measurements are divided in two parts. This report includes measurements with and without cooling. The second part contains measurements with the former cooling configuration and air jet vortex generators (AJVG´s), additionally. The second report will be delivered at the end of the project. The profile contour was designed by RRD and handed over at the beginning of the project. Besides do other partners numerical simulations for these flow cases.
The following measurement techniques are applied:

- Schlieren technique
- Infrared thermography
- Hot-wire anemometry
- Pressure tapping's
- Wake traverses

The hot-wire anemometry was deployed to investigate the inflow conditions. These results were already handed over to the partners, who adopt the numerical part, for their inlet boundary conditions. The measurements are utilized to compare them with the numerical results.
This report is subdivided in the description of the wind tunnel system, the metrology, a subsequent chapter about uncertainties estimations and the presentation of the measurements will be done in the chapter Results and Discussion.

German Aerospace Center

Site Göttingen
Institute of Propulsion Technology
Department Turbine

Contents

Experimental Set-up

1. Test facility

The measurements are performed at the Wind Tunnel for Straight Cascades at the German Aerospace Centre in Göttingen. The wind tunnel operates in a closed circuit. The air is driven by a 3.7 MW compressor. The compressor achieves a maximal pressure ratio of 14 and a volumetric flow of 60000 to 230000 m³/h.

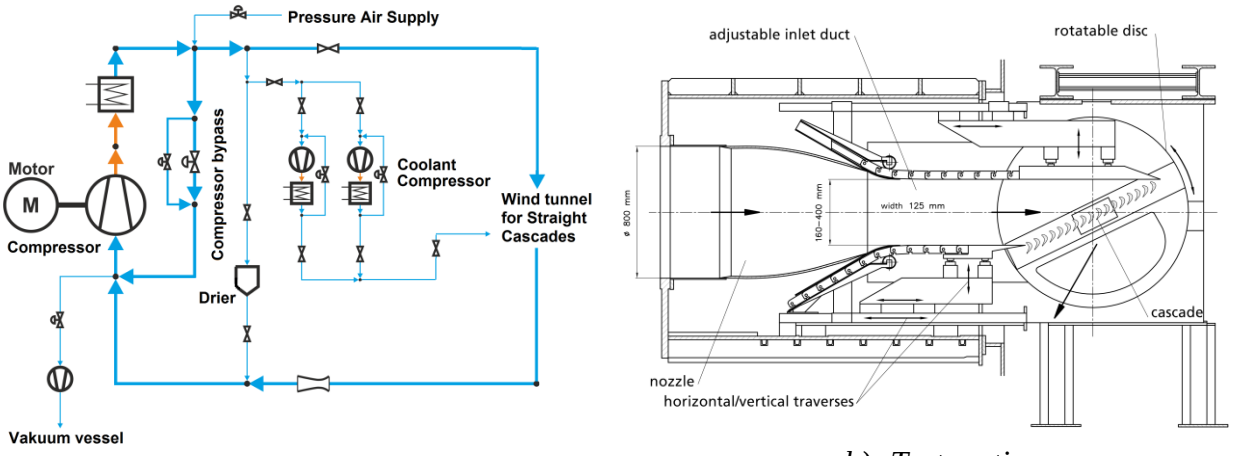

a) Schematic view of closed circuit

b) Test section

Figure 1 Wind tunnel for straight cascades

Figure 1 (a) shows a schematic view of the closed circuit. On the right side is the Wind Tunnel for Straight Cascades (EGG). The compressor is shown on the left side. The whole system will be evacuated at the start of a test run. After achieving a certain pressure in the system the compressor can be started. Subsequently, the system will be filled up with dried air. Additional drying is done while operation. The compressor exit air has a temperature of approximately 200°C. It is cooled behind the compressor. Therefore it is possible to control the pressure and temperature at the inlet of the test section. The air for the cooling flow is taken behind the pressure air supply. The pressure of this air can be enhanced if required.

Figure 1 (b) shows the test section of the EGG. The air is accelerated through an adjustable duct into the test section. The cascade is installed on a rotatable disc. If required the inlet angle might be adjusted. The height of the cascade is bounded by adjustable walls. The maximum height is 400 mm. The channel width is fixed at 125 mm. The exhaust flow enters a plenum behind the test section. It passes a diffuser behind the chamber plenum. The diffuser is adjustable and adjusts the chamber pressure. Therewith the turbine exit Mach number will be controlled.

The coolant supply delivers air through one pipe. It ends in the test section in a distribution box. The box has up to ten outlets. In this box is a thermocouple which gives the temperature of the coolant flow. The distance of the distribution box to the blade is approximately 2 m. Three blades are connected to the cooling supply. This includes the measurement blade and both blades next to it. The measurement blade is coloured in Figure 2 (c). Further definitions about this Figure are given in the next subsection.

2. Cascade and cooling geometry

In this work package three types of high pressure stator blades are investigated. The profile contour is the same for every blade type. Solely, the blowing of the blade will be adjusted. This report contains the first two blade types. The profile design was performed by Rolls-Royce Deutschland (RRD). Table 1 lists the geometric cascade parameters.

Table 1 Geometric parameters of cascade

chord length [mm]	**75**
pitch [mm]	**68.2**
axial chord [mm]	**34.66**
throat [mm]	**14.56**
blade height [mm]	**125**
Stagger angle [°]	**31.72**

Additionally, RRD delivered the specifications of the cooling blade which is the second blade type. These are shown in Figure 2 (a) and (b).

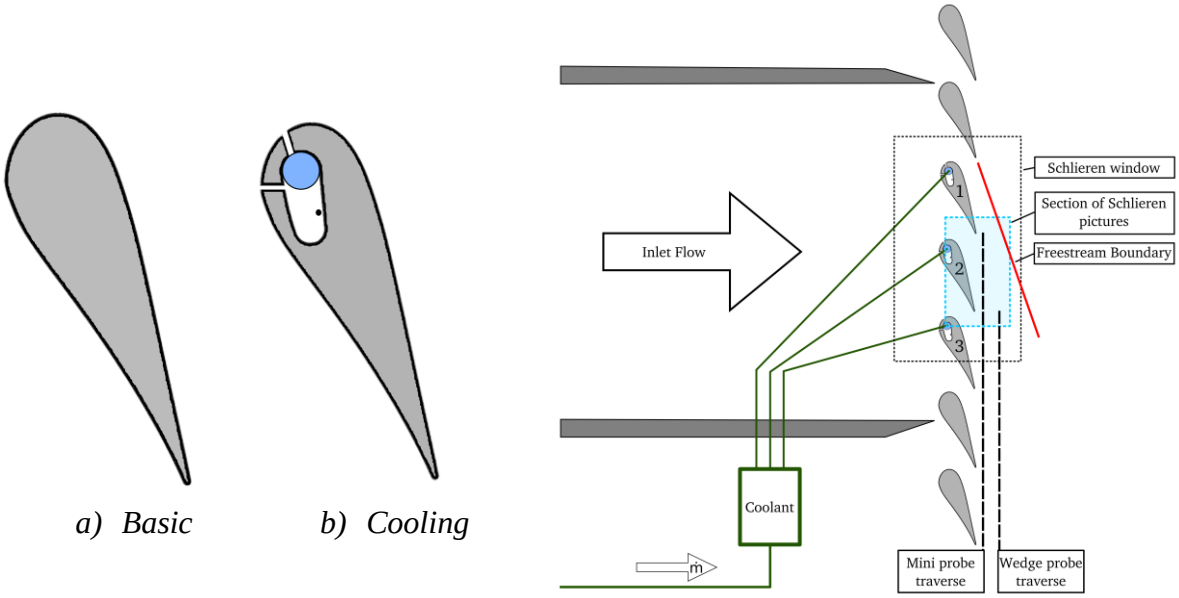

a) Basic *b) Cooling* *c) Cascade*

Figure 2 TFAST profile and cascade

The basic blade has no cavity and no blowing orifices. The cooling blade has one cavity and two cooling rows. In Figure 2 (b) the mass flow supply area is highlighted in blue. A black dot in the cavity highlights the location of a pressure probe. The lower row at the nose of the blade is named “Row 1”. The designation of the other row is “Row 2”. The diameter of the supply pipe is at the minimum 7.48 mm shown in Figure 2 (b) by a red solid circle. A black dot at the lower part of the cavity in shows the position of a pitot probe. It ends at the spanwise mid of the cavity.

Figure 2 (c) shows a sketch of the test section and the TFAST cascade. Due to the small stagger angle and a long chord five blades remain in inflow area. The blade with number 2 is denoted as the measurement blade. The numbers designate the wake traverse measurements to the blades. Later explanations about the metrology will refer to this designation. Additionally, the rough position of the Schlieren window is shown through a black solid line. The blue dashed line shows the section of the Schlieren pictures, which are shown in the results. The freestream boundary is highlighted by a red solid line. At the cooling case three blades equipped with the cooling cavity were installed. These were installed at the position of the measurement blade and at both sides of it. Additionally, the distribution box of the coolant supply is shown. Further specifications about the coolant rows are listed in Table 2 and Figure 3.

Table 2 Geometric quantities of coolant rows and holes

Coolant Row	*Row 1*	*Row 2*
Hole diameter [mm]	**0.9**	**0.9**
Hole distance/Hole diameter [-]	**2.5**	**2.5**
Hole length/Hole diameter [-]	**≈ 5**	**≈ 5**
Number of holes [-]	**46**	**46**
Span of row [mm]	**101.24**	**101.24**
Coolant area [$10^{-4}m^2$]	**1.17**	**1.17**
Hole angle [°] (bitang.)	**90**	**16.25**
Hole angle [°] (axial)	**0**	**0**
Radial hole angle [°]	**0**	**0**

The ratio hole length/hole diameter is designed as suggested in Lutum1999, Jung2001 and Burd1999. The tube flow should be fully developed if this ratio has an amount of 5.

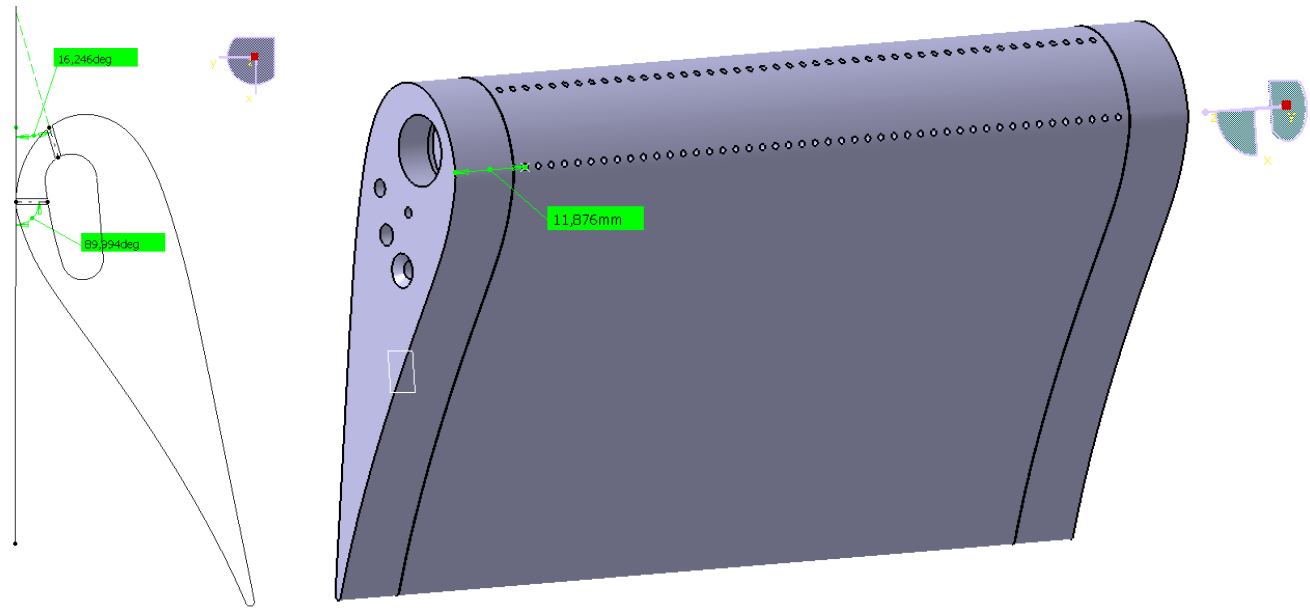

Figure 3 TFAST Profile with cooling cavity

The tuning of the cooling parameters is done by the cavity pressure in the Measurement blade. The specifications were given by RRD and these are listed in Table 3.

Table 3 Coolant flow configurations

cm [%]	*Cavity pressure [kPa]*	*Mass flow [g/s]*	*Discharge coefficient [-]*
0	**-**	**-**	**-**
1.1	**120.7**	**13.3**	**0.48**
1.4	**126.5**	**17.1**	**0.49**

It gives the cavity pressure and the mean mass flow of the supply pipe at the wake measurements. Additionally, the resulting discharge coefficient is shown at the different cooling configurations. The average temperature in the distribution box was averaged to 297 K.

Metrology

In this chapter the applied measurement techniques and its approaches are described. In the first subsection are two techniques summarized. These are the techniques which are applied at the investigation of the inlet conditions. For this purpose a 1D hot-wire-anemometer and a 3 hole probe were applied. Further are described the infrared thermography, Schlieren technique and wake traverses. On one blade were installed 20 pressure taps and on another blade a hot-film element with 28 wires.

Figure 4 shows the blade and the normalised geometric dimensions. The positons of the pressure taps and the hot-film wires are shown next to the positions of the coolant orifices.

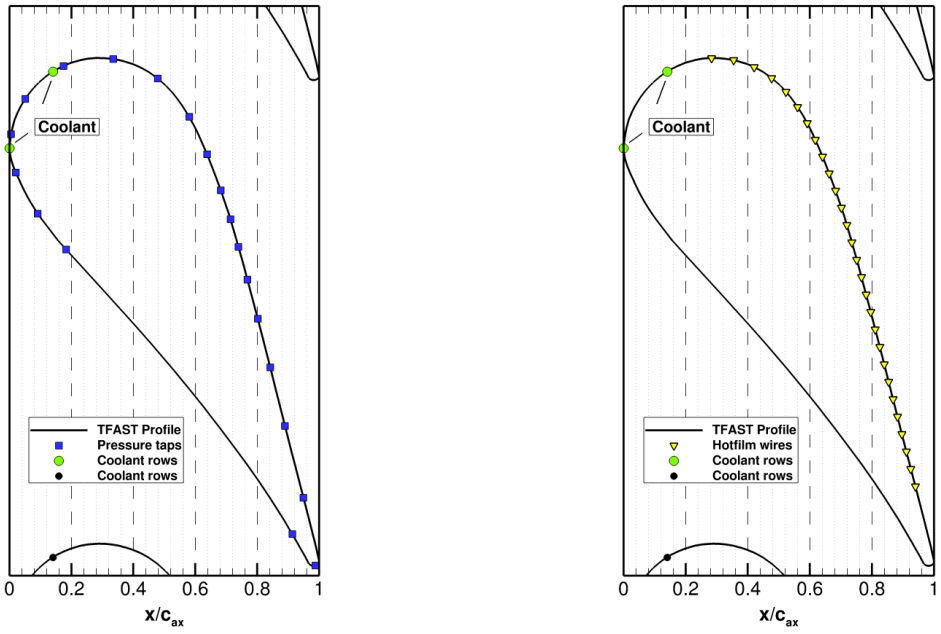

Figure 4 TFAST Profile, position of coolant rows, pressure taps and hot-film wires.

1. Inlet measurements

To determine the boundary layer thickness at the wind tunnel side walls and the fluctuating data at the inlet plane of the test section two different measurement methods were applied. These are a hot-wire probe and a cobra probe. Both probes were moved span wise between a wall and mid-span with the help of a traverse mechanism.

The 1D hot-wire probe Dantec 55P11 is applied by using a 5 µm tungsten wire. It is operated with the StreamLine 90N10 Frame.

The turbulence intensity (*Tu*) is determined with this equation:

$$Tu = \frac{\sqrt{u'^2}}{\bar{u}}.$$

For this calculation is applied a windowing of approximately 1000 values for each measurement. The resulting turbulence intensities are afterwards averaged.

Infrared thermography

The infrared measurements are performed with a Nikon Laird S270A. A Stirling circle cools a PtSi Schottky-Barrier IR CCD sensor. It´s resolution is 475*442 pixels. The sensitivity of the camera is in the range of 3 to 5 µm. The frame rate can resolve 30 Hz in an observable temperature range of -20°C to 250°C. The accuracy given by the manufacturer has a temperature of ± 2K [Nikon2000].

The infrared camera was installed behind the Measurement blade. Figure 5shows the temperature distribution of the suction side.

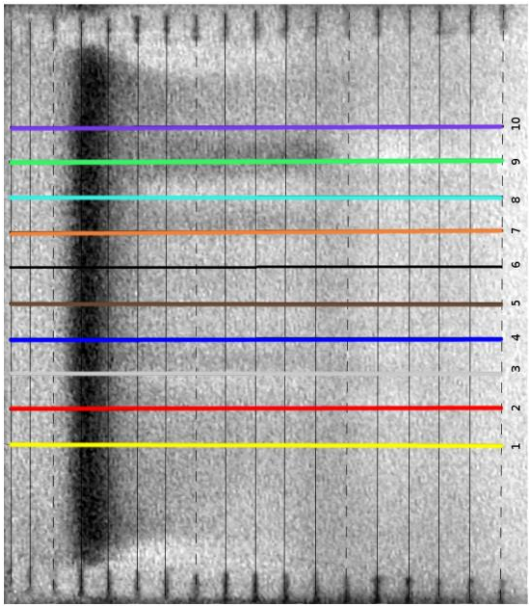

Figure 5 Evaluation of infrared pictures, Basic case

Markers are engraved to relate the measurement and the spatial resolution. These markers are positioned close to both side walls. Connecting the markers gives the spatial resolution in flow direction. For data reduction ten lines were extracted. The extracted lines start at the highest marker line down to the lowest one close to the trailing edge. The ten extracted lines are averaged. The relation of the pixels and the marker lines is linked by a polynomial function. The correlation coefficient for this function has an amount of 0.99. The same approach was applied for the cooling measurements.

The applied evaluation approach is based on the description of Fey2006. Two infrared images are recorded during measurement operation at a frequency of 30 Hz. The first one was taken at 299.5 K ($_{cold}$). Afterwards, the inlet temperature was raised at constant exit Mach number. The second image was taken at approximately 300.5 K (T_{heat}). The presented result is a division of T_{heat}/T_{cold}. The temperature step was not kept constant in each measurement. Therefore, normalization is done by a division with the temperature ratio at the smallest relative axial chord. Hence, the shown result T_{ratio} will be calculated as follows:

$$T_{ratio} = \frac{\frac{T_{heat}}{T_{cold}}}{\left(\frac{T_{heat}}{T_{cold}}\right)_{c_{ax}=46\%}}.$$

Schlieren visualization

The arrangement of the Schlieren visualisation at the wind tunnel for straight cascades is conventionally and shown in Figure 6, Kost2004. The light source is a flash lamp of the company Nanolite (rare gas: Argon). The flash light pulses with a length of 20 µs.

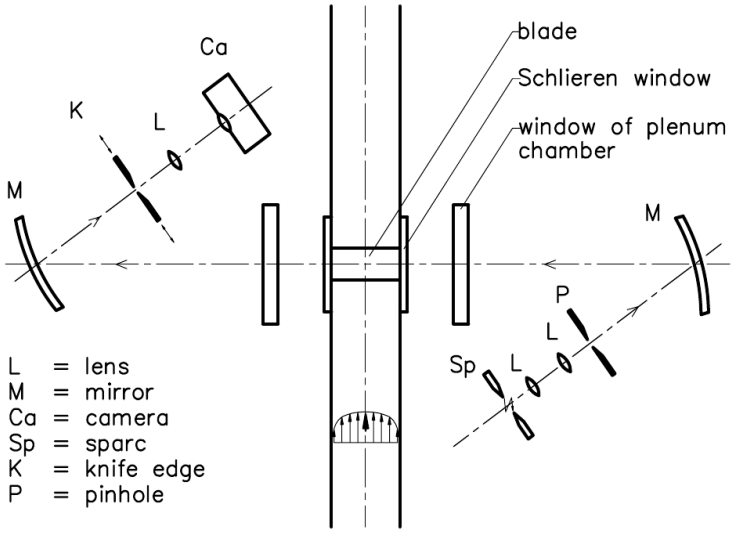

Figure 6 Schlieren arrangement, Kost2004

The camera is a Canon EOS 7D with a CMOS sensor. It´s resolution has 2496*3420 pixels. An ISO speed of 160 and a shutter speed of 1/400 were applied.

2. Flow field pressure measurements

A blade equipped with 20 pressure taps was applied for the surface pressure distribution. The diameter of each pressure tap is 0.3 mm. The exit flow conditions were investigated with two multi hole probes. With a relative axial distance of 11.54 % to the blade trailing edge plane a 4-hole Mini probe was deployed. 51.91 % behind the trailing edge plane a 3-hole Wedge probe was installed. The wake traverses are depicted in Figure 2 (c). In Figure 7 is shown a sketch of the probe heads. Additionally, the traverse positions are outlined. Further information about the probe and its calibrations are described in Kost2009 and Ren2010. The resulting experimental uncertainties (error bars, basing on a 95 % confidence level) of the wedge type probe for wake traversing are evaluated within a range of 0.01 for the Mach number, about 0.5° for the flow angle, and about 0.002 for energy loss coefficients [Rehder2012].

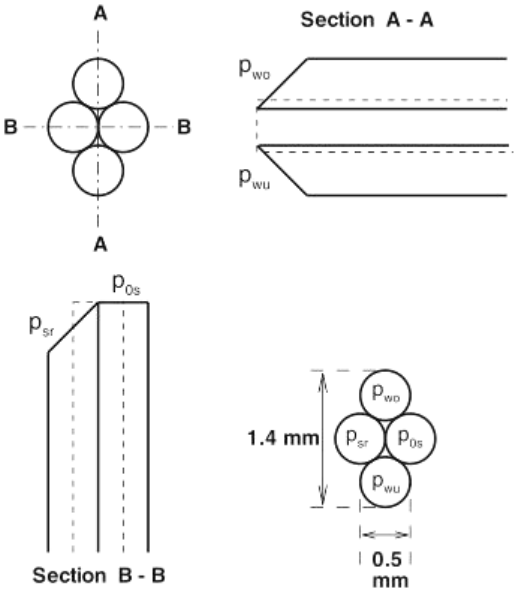

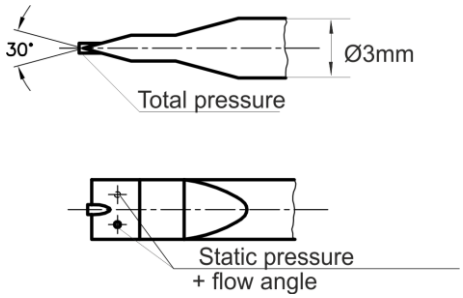

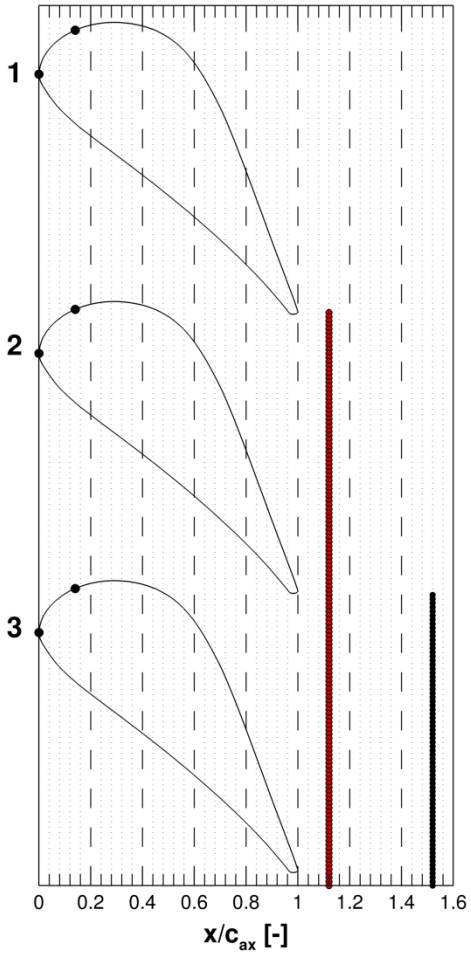

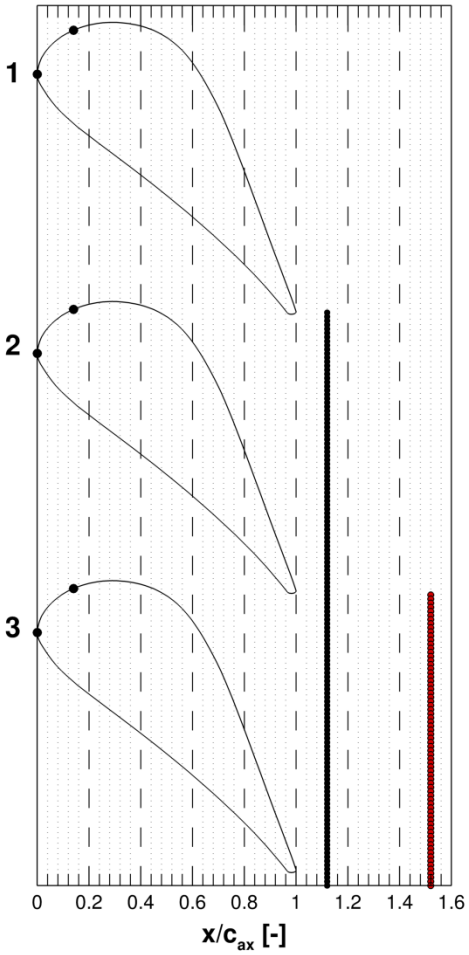

Mini probe, Ren2010

Wedge Probe, Kost2009

Figure 7 Multi hole probes

The traverse is discretised by a step size of 1 mm. The lower part of Figure 7 shows the start positions for the wake positioning for each probe. The measured inhomogeneous data are recalculated to the homogeneous data by applying the equations of conversation of mass, momentum and energy, Amecke1995.

The aerodynamic loss (ξ_S) is calculated according to Kiock1985. The mass flow coefficient is ignored for the calculation of the aerodynamic loss. This was done because all blade flows have the same total temperature than the inlet temperature. Hence, an influence of the enthalpy is not expected. The main focus lays on the influence of the aerodynamic:

$$\xi_S = 1 - \frac{1 - \left(\frac{p_2}{p_{02}}\right)^{\frac{\kappa-1}{\kappa}}}{1 - \left(\frac{p_2}{p_{01}}\right)^{\frac{\kappa-1}{\kappa}}}.$$

The given losses are the homogeneous data around the wake of the measurement blade (2 in Figure 2 (c)). The homogenization reaches half pitch in each direction of the measurement blade.

The pressure data were gauged by PSI 8400 of the company Pressure Systems. A schematic view of the measurement chain is shown in Figure 8. The pressure sensors are silicon piezoresistive sensors. The calibration unit determines at the beginning of each measurement day a 4th order polynomial function for each pressure port. The ESP scanner is not temperature compensated and changes in ambient temperature have to be considered in the error calculation. The static accuracy is ± 0.05 %, the thermal zero error is ± 0.06 %/°C and the thermal span error ± 0.02 %/°C. At this measurement one has to apply a temperature delta of 10°C and the total error results to ± 0.85 %.

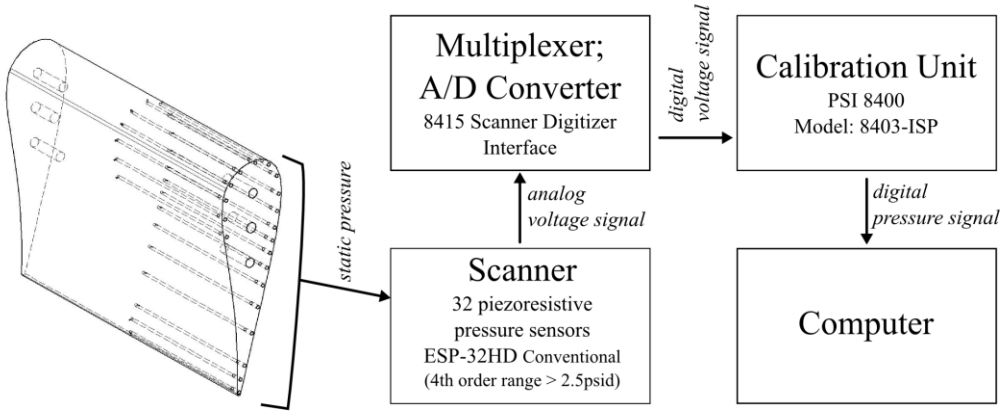

Figure 8 Schematic view of pressure measurement chain

3. Massflow measurement

The massflow is measured at one pipe of the coolant supply. The pipe leads to a distribution box in the test section. This is already described in chapter Experimental Set-up. The massflow is determined with an orifice plate consider the standards of DIN EN ISO 5167-1/2 (2003). For the temperature measurement was applied a K-Type thermocouple of the company Temperatur Messelemente Hettstedt GmbH. The mineral insulated thermocouple

has a diameter of 6 mm. The connected multimeter (3706) and screw terminal (3724-ST) are manufactured by the company Keithley Instruments Inc.. The Co-Junction-Compensation (CJC) is integrated. The pressure data were gauged by PSI 9010 of the company Pressure Systems.

With the help of the massflow measurement is the mass flow coefficient calculated [Kiock1985]. Therefore it is primarily necessary to calculate the passage massflow:

$$\dot{m}_h = \frac{h_c}{h} \cdot \left(\frac{2}{\kappa+1} \right)^{\frac{\kappa+1}{2\cdot(\kappa-1)}} \sqrt{\frac{\kappa}{R}} \frac{p_{01}}{\sqrt{T}} A_{passage}.$$

The area $A_{passage}$ includes the channel width were coolant holes ejecting coolant massflow $\dot{m}_c$. The massflow of each blade $\dot{m}_c$ is a third of the measured massflow. The mass flow coefficient c_m is determined as follows:

$$c_m = \frac{\dot{m}_c}{\dot{m}_h}.$$

4. Hot-film element

On a cooled blade has been installed a 28-nickel wire hot-film element. The limitations were given by the coolant rows and the trailing edge. Figure 9 shows two views of this blade.

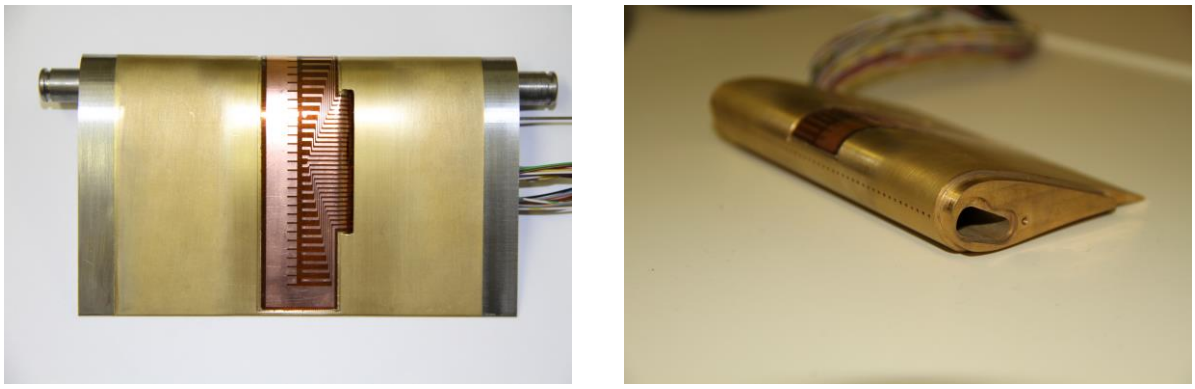

Figure 9 Cooling blade equipped with hot-film element

The hot-film element was manufactured by Tao of Systems Integration, Inc.. The leads with a height of 12.7 µm together with the 0.2 µm nickel wire on a 50 µm high polyimide film were glued with a 130 µm thick gluetape in a 0.2 mm deep pocket. Figure 9 shows the hot-film on the blade. After completion, the hot-film element edges were filled with filler to ensure a smooth transition to the blade.

The length of the hot-film sensors is 1.45 mm and the width is 0.1 mm. The sensors are equally spaced on the hot-film element with a distance of 2.5 mm. The leads were let in the blade. Inside the blade are the cables soldered on the leads. All cables exit the blade on one side and are connected outside of the test section to a multiplexer. The multiplexer has four output channels and is connected to four modules of the Dantec StreamLine 90N10 Frame. The analog signals of the hot-film are digitalized with an A/D converter and send to a computer. The measurement chain is visualized in Figure 10.

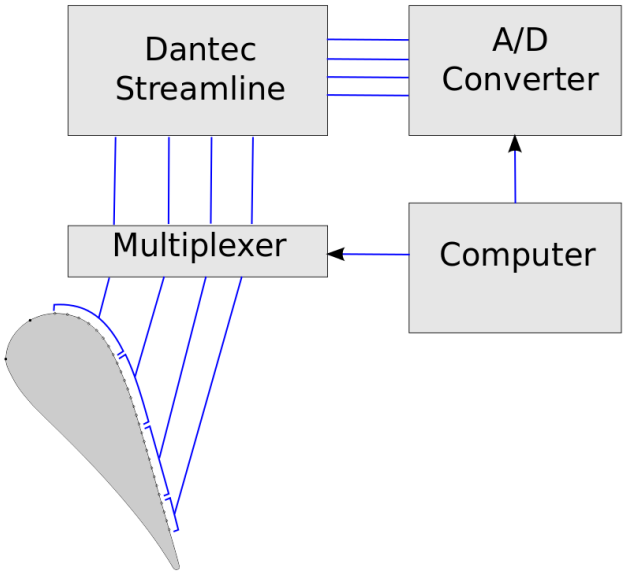

Figure 10 Schematic view of hot-film measurement chain

The ground wire of the hot-film is summarised to one. At other cases it was possible to measure a few hot-film-wires parallel. In this case was the mutual influence to high and all hot-film-wires were measured at different times. The evaluated data are the fluctuating voltages:

$$U' = U - \bar{U}$$

Out of the fluctuating voltages has been calculated the root mean square

$$Rms = \sqrt{\frac{1}{N}\sum_{i=1}^{n} U'^{2}_{i}} \,,$$

and the skewness. The calculation of the skewness is described in Zwillinger2000.

Results and Discussion

This chapter treats the results of the applied measurement techniques. These are subdivided in different subchapters. The metrology has been described previously. Hence, the following chapters are solely describing the gained data.

5. Inlet Measurements

The location for the inlet measurements is 80 mm upstream of the blade nose. At discrete locations hot-film data were recorded. The results of the calculated Turbulence intensity are shown in Figure 11.

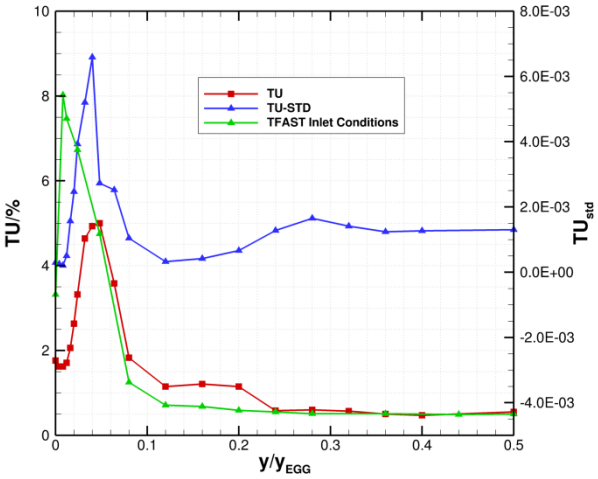

Figure 11 Inlet measurements: Turbulence intensity

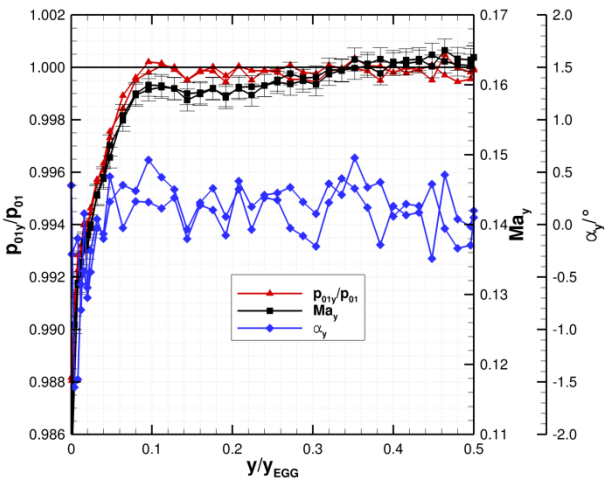

Figure 12 Inlet measurements: Pressure distribution

The data in Figure 11 are plotted over the relative channel width. The hot-wire anemometer measured from one wall to the midsection. In Figure 11 are compared the turbulence intensity of the blow down operation with the operation at closed circuit with the compressor. The development of both is at the midsection approximately the same. Reasons for the revealed differences cannot be named. The standard variance is calculated from the data of operation at closed circuit. The highest variances occur at the boundary layer. The turbulence intensity show both the height of the boundary layer at the channel wall. It´s edge can be found at 0.12 relative channel height. Figure 12 shows the results of the Cobra 3-hole pressure probe. These data were acquired at the same distance to the blade as the hot-wire data.

Shown are the normalized data and the probe Mach number with its errors. Since the probe is a 3-hole probe the Alpha angle data are displayed, additionally. The results for the angle are close to zero. For the velocity fluctuations of the hotwire data a FFT is applied. The power spectra are shown in Figure 13.

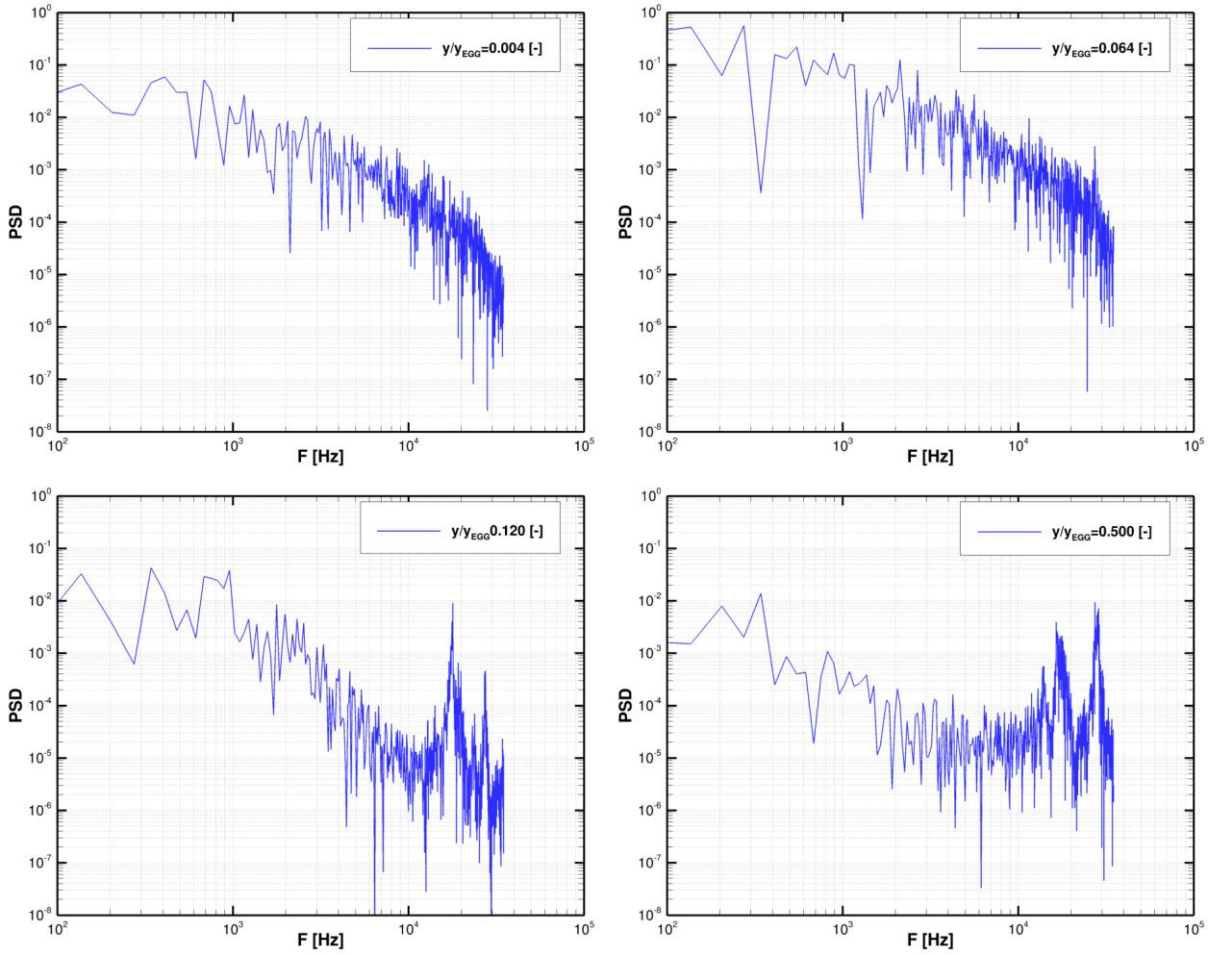

Figure 13 Power spectra of inlet hot-wire data at discrete positions

For Figure 13 were chosen four measurement locations of the data obtained while compressor operation. Outside of the boundary layer appear in the range of 15 to 30 kHz two peaks. Their appearance cannot be explained with vortex shedding of the hot-wire probe nor its holding rod. The blade passing frequency is lower. Hence, this is no explanation for the peaks.

6. Flow field measurements

This chapter contains different measurement techniques to obtain information about the flow field. These include Schlieren technique, surface pressure distribution and wake traverses.

In Figure 14 the results of Schlieren technique are shown. Figure 14 (a) shows at the basic case and (b) to (d) at different massflow rates of the cooling blade. The alignment of the knife edges is shown in each picture.

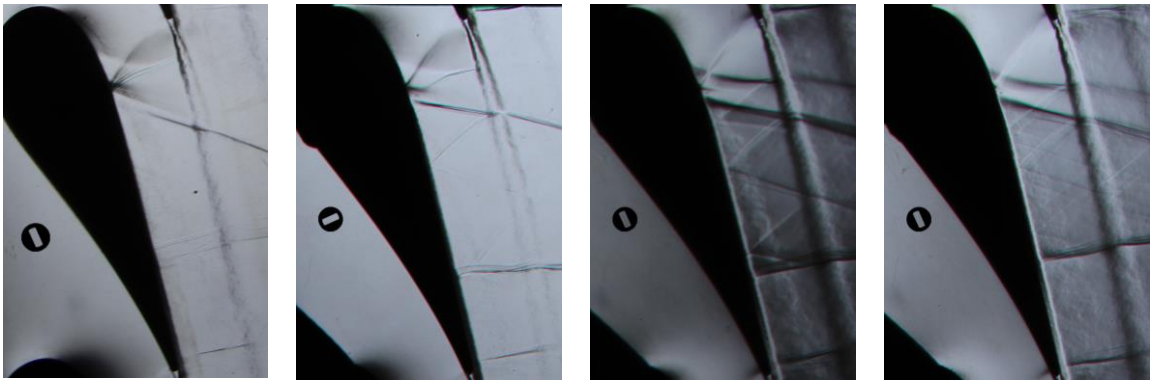

d) Basic *e) Cooling, c_m = 0%* *f) Cooling, c_m = 1.1%* *g) Cooling, c_m = 1.4%*

Figure 14 Results of Schlieren technique

The incident shock at the passage is reflected on the suction side. Upstream of the incidence shock impinging point indicates the so called separation shock [Figure 15, Babinsky2011] the beginning of a separation. This shock reflects at the upper wake. This reflected shock is nearly normal. Downstream of the shock impinging point a reattachment shock indicates the separation completion. Downstream of the passage is a normal shock shown and even closer to the trailing edge a weaker second normal shock. These normal shocks are unsteady. This revealed the comparison of different pictures.

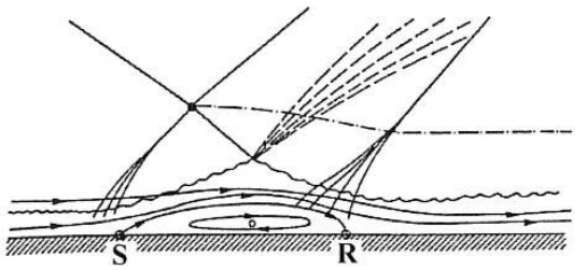

Figure 15 Shock reflection with separation, Babinsky2011

Figure 14 (b) shows similar behaviour. The apparent differences might be induced by the unsteadiness of the flow field. Figure 14 (c) shows a difference of the separation shock. It´s initial point is closer to the incidence shock impingement point. This distance is even smaller in Figure 14 (d). Additionally, the reflection on the wake is further downstream in (c) and (d) than in the cases without cooling flow. This leads to an oblique reflection. One has to keep in mind that the flow is at that point already unsteady. An analysis with the help of the other techniques will reveal more precise information.

The reflection of the incidence shock is obviously an expansion wave. This is another indication for a separation in all pictures of Figure 14. The flow behaviour is comparable to the sketch in Figure 15.

The reflections of the separation and the reattachment shock propagate downstream until the appearance of the normal shock terminates them. Besides, at the cooling blade (Figure 14 (b) – (d)) is an increase of the boundary layer behind the transition visible. The thickness of the boundary layer increases distinctly with the normal shock. The second normal shock at the trailing edge seems to have no influence on the boundary layer thickness.

Figure 16 shows the surface pressure distribution. There are two exit Mach numbers shown. Additionally, next to the Mach number is shown the pressure distribution. The symbols of the Mach number distribution are connected with lines to give a better overview in the graph. The lines do not show any obtained results. The error ranges due to errors of PSI system are denoted as well.

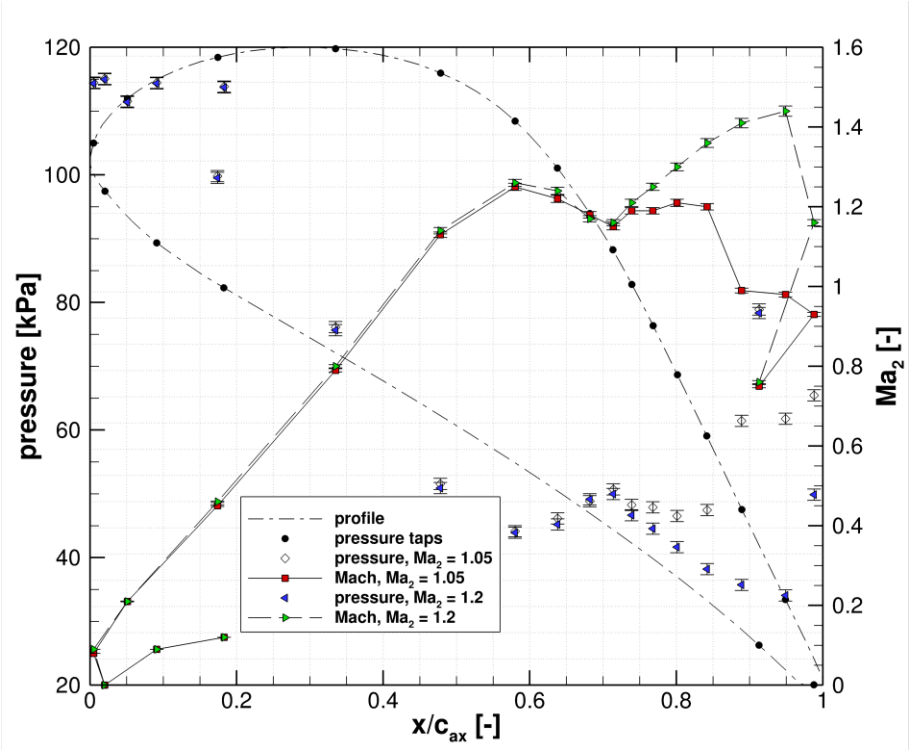

Figure 16 Pressure and Mach number distribution, Basic case

The additional Mach number 1.2 was measured to show the pressure distribution of only one shock downstream of the passage. This was asked by the Partners because the numerical simulations show the appearance of one shock downstream of the passage close to the trailing edge. The strong normal shock Figure 14 (a) moved to the trailing edge and changed to an oblique shock due to higher exit Mach number.

Besides, the results for exit Mach number 1.05 show a good agreement with Figure 14 (a). All shocks which appear in the Schlieren picture appear in the pressure distribution as well. More precise information could be achieved with the help of a higher discretisation of the pressure taps.

Figure 17 shows the result of the Wedge probe. It was installed further downstream of the blade than the Mini probe (Figure 7). The relative wake traverse positions (y-y_0/t) refer to the numbers shown in Figure 2 (c). The start position for the Mini probe is set to 1 behind the trailing edge of the upper blade (1 in Figure 7). Besides, the start position (y-y_0/t = 1) of the Wedge probe is set one pitch lower.

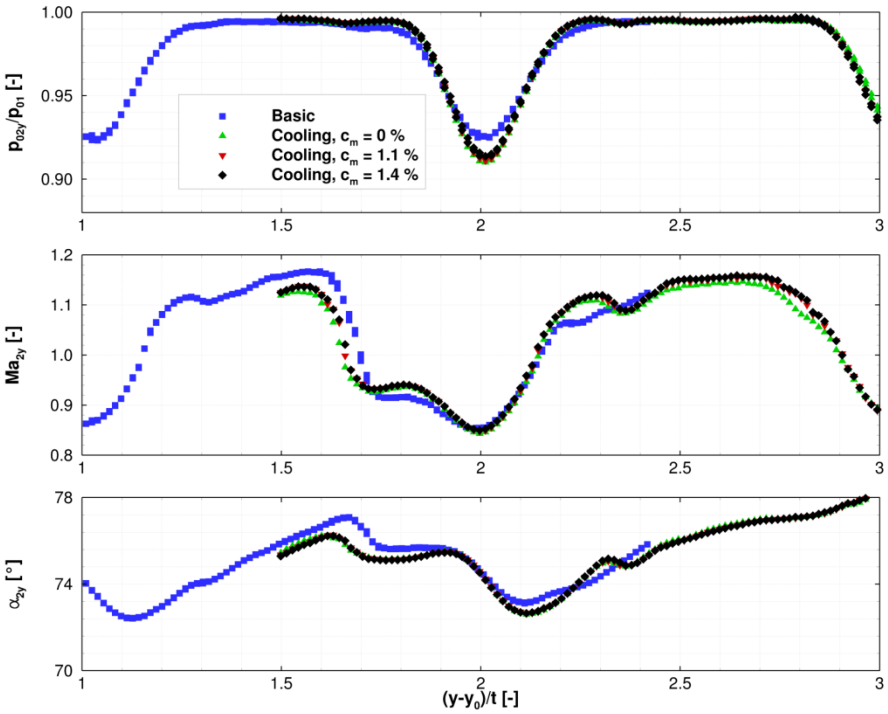

Figure 17 Wake traverse, Wedge probe

One sees at the top the relation of probe pressure p_{02y} to inlet pressure p_{01}. The probe Mach number Ma_{2y} is shown below and at the bottom of Figure 17 the circumferential angle α_{2y}. A distinct difference is shown between the two blade types. Besides, the coolant case without coolant flow shows another Mach number course. This indicates divergent shock behaviour. The wake at the basic blade is less sharp than the coolant blade.

Figure 18 shows the results of the Mini probe traverses. An extra hole enables the measurement of the radial angle. Due to a smaller probe head the distance to the cascade was decreased to 4 mm.

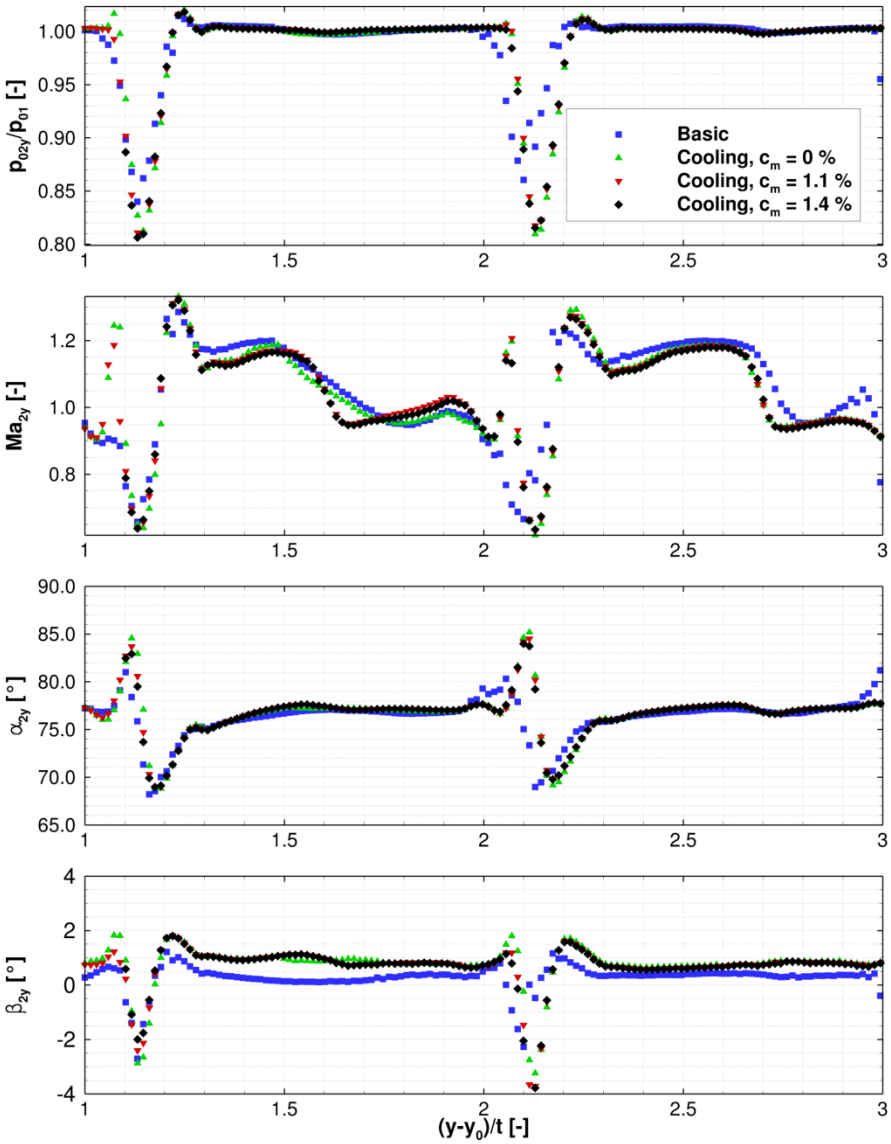

Figure 18 Wake traverse, Mini probe

The total pressure ratio shows sharper wakes than it was acquired with the Wedge probe. The Mach number distribution does reveal a broader distribution of the normal shock. The position of the normal shock differs between the cases without and with coolant flow. A shift of the circumferential and the radial angle can be found between the cascades. These are small enough to be caused by installation and manufacturing tolerances.

In the next Figure 19 are shown the losses calculated of the inhomogeneous measurements obtained with the Wedge probe. The evaluated position is $y\text{-}y_0/t = 2$.

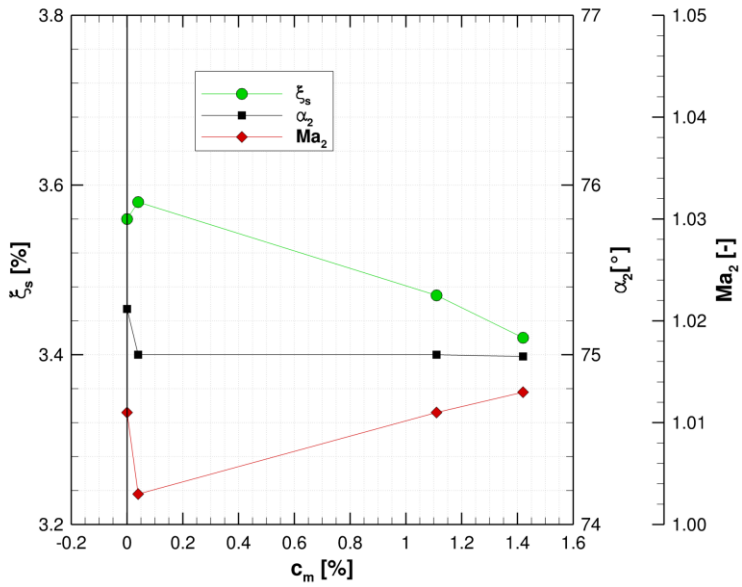

Figure 19 Losses, exit angle, mixed out Mach number of Wedge probe measurements

The aerodynamic loss ξ_s decreases with the introduction of a coolant cavity. The coolant cavity has two blowing rows which are connected through the cavity (Figure 2 (b)). One of these rows is located at the blade nose in flow direction. Hence, at this location is the highest static pressure. The other coolant row exits at a strongly accelerated location. The higher pressure in the cavity succeeds at the acceleration region, which results in a small mass flow. As soon as the coolant air is introduced to the flow does the aerodynamic loss decrease. This trend continues with higher coolant mass flow. The exit circumferential angle decreases with the introduction of coolant. Afterwards are no changes in the exit angle observed with the increase of coolant mass flow. The homogenised exit Mach number increases with coolant flow.

7. Transition detection techniques

This chapter shows the results of the wall temperature distribution measured by an infrared camera and hot-film data. Both techniques are applied for transition detection.

Figure 20 shows the temperature distribution of the basic case and the cooling blade with all blowing ratios on the suction side. The upper edge is approximately at the relative axial chord position 0.45. The lower edge coincides with the trailing edge of the blade. The colour map fits for every picture separately. For the infrared measurement were added markers into the blade surface near both walls. The sidewall effects are stronger caused by the markers for the positon tracking. In Figure 20 are these markers highlighted by a white connecting line. Every fifth line is dashed for a better overview.

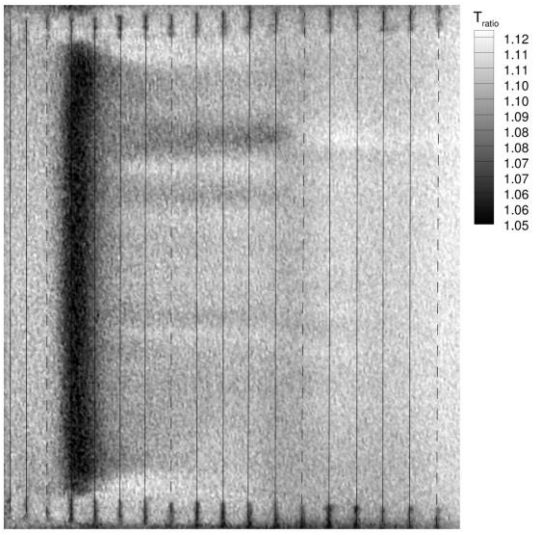

h) Basic

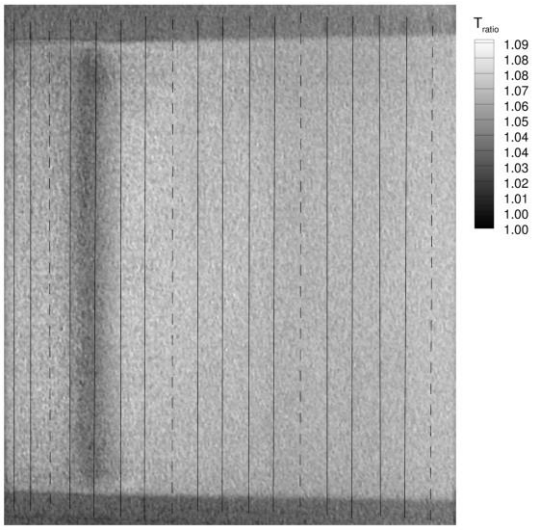

i) Cooling, c_m = 0%

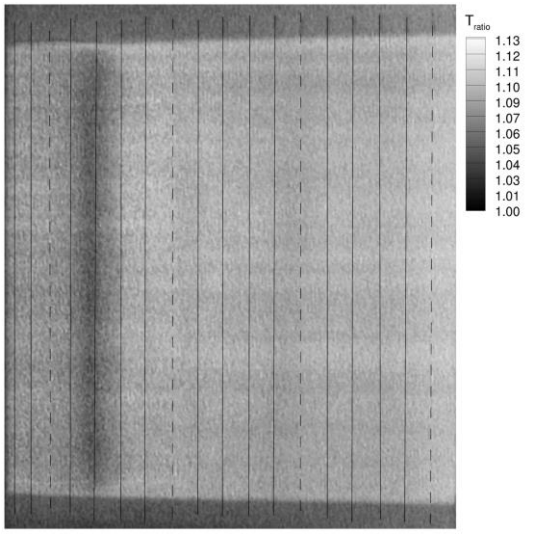

j) Cooling, c_m = 1.1%

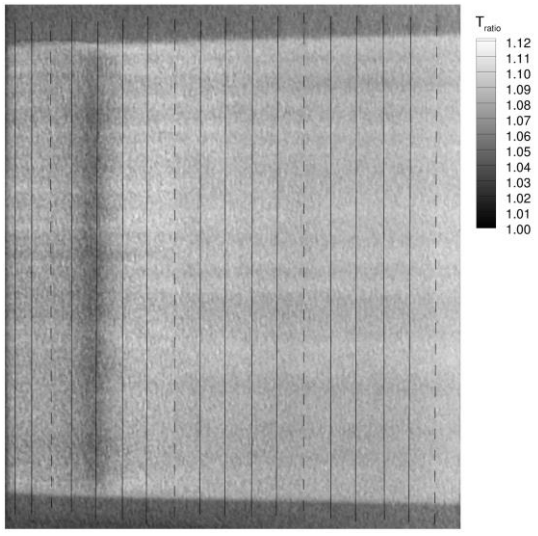

k) Cooling, c_m = 1.4%

Figure 20 Temperature distributions on suction side

All pictures in Figure 20 have at the upper region the coldest temperature ratios. This upper region is located at the end of the acceleration region (see Figure 16). Afterwards, the temperature starts to rise. Between the basic and the cooling case are differences. In Figure 20 (a) one can perceive turbulent wedges. These are distorted in Figure 20 (b) – (d) by the coolant holes. The colour becomes bright in all pictures at the third dashed row in streamwise direction. Subsequent an evaluation of the temperature distribution will be compared with the pressure distribution.

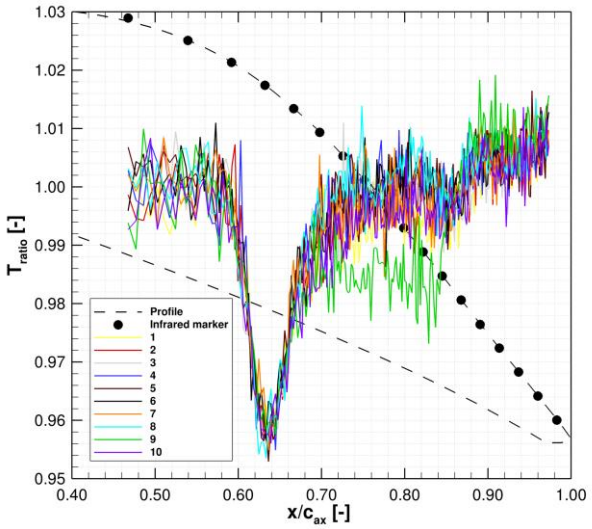

Figure 21 Discrete temperature distributions of basic case

Figure 21 depicts normalised temperature ratios of the basic case. Ten of them are extracted at different locations. These are outlined in in Figure 5. The temperature descends until the curve reaches its minimum at $x/c_{ax} \approx 0.64$. This deflection indicates a separation. The introduced temperature rise is not able to increase the wall temperature. The assumption in this case is the appearance of a separation. The separation operates in this case like an insulator. Behind the deflection rises the curve until $x/c_{ax} \approx 0.9$. At this position appears a leap up to a higher temperature ratio. This indicates the appearance of transition. In Figure 21 one line is outstanding. Behind the separation remains this line at a distinct lower level until $x/c_{ax} \approx 0.9$. This indicates a laminar state until the temperature gradient rises up again. In the next Figure 22 are all cases averaged over the ten lines for each case and shown next to the Mach number distribution. Additionally, the blade profile geometry with infrared markers is shown.

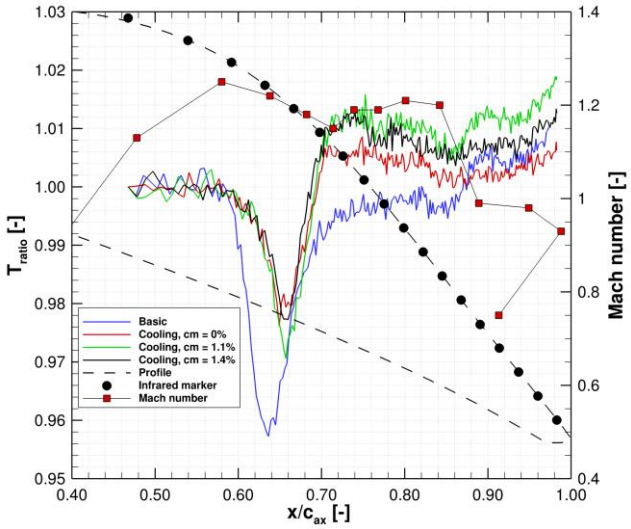

Figure 22 Averaged temperature distributions of all cases and Mach number distribution

The lines are drawn between the pixels. A smoothing in flow direction was renounced. The onset of transition is at the basic case earlier than at the cooling cases. Furthermore is the temperature ratio level behind the separation higher than at basic case. This indicates a transition process. The strong normal shock at $x/c_{ax} \approx 0.9$ does introduce a minor rise of the

temperature level at the cooling cases. This might be interpreted as a thickening of the boundary layer. But the transition process seems to be completed. A significant reduction of the separation size is not revealed.

The next figure shows the results of the hot-film measurements. For the evaluation process was used uncalibrated voltage data. In Figure 23 are shown 100 ms of the fluctuating voltages. One has to keep in mind that those data are not recorded at the same time.

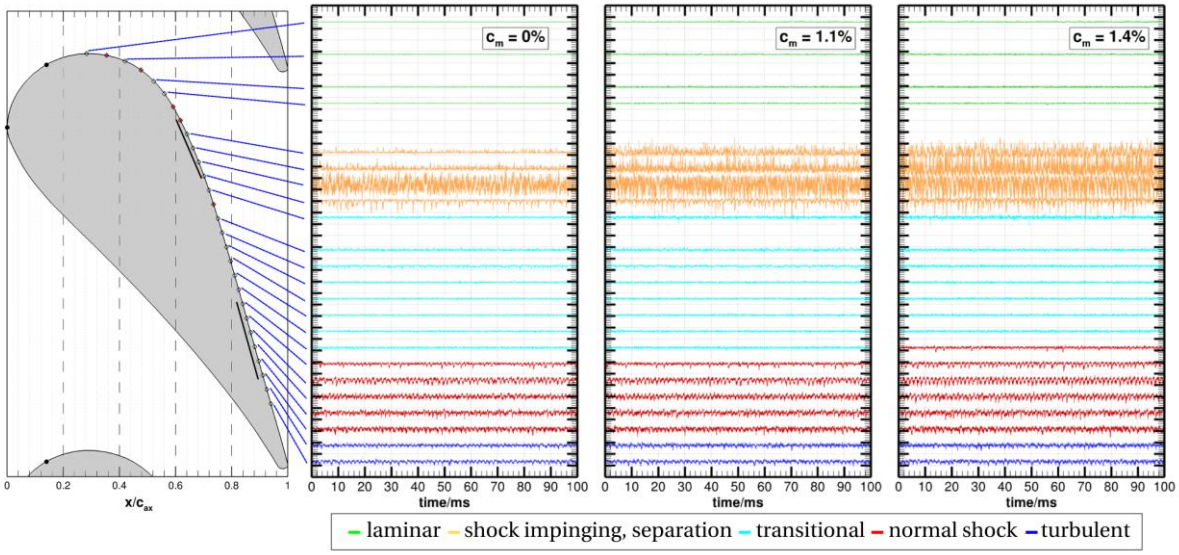

Figure 23 Time signals of fluctuating hot-film voltages

Some of the hot-films fall victim at the manufacturing process. These are outlined in red on the left side in Figure 23. The usable wires are connected to the fluctuating voltages by blue lines. In the blade are highlighted with black bold solid lines the positions of separation and shocks. Additionally, the time signals are coloured by boundary layer state and shock interacting regions. This information is taken from infrared and pressure data, as well as from the Schlieren technique.

The separation region produces major amplitudes. A comparison of all three measurements at different coolant mass flow ratios reveals a remarkable influence of the coolant. An increase in the fluctuations due to the appearance of the normal shock downstream of the passage can clearly be seen. An easier comparison of these data will be done in Figure 24. The fluctuating voltages are calculated to Rms and Skewness data.

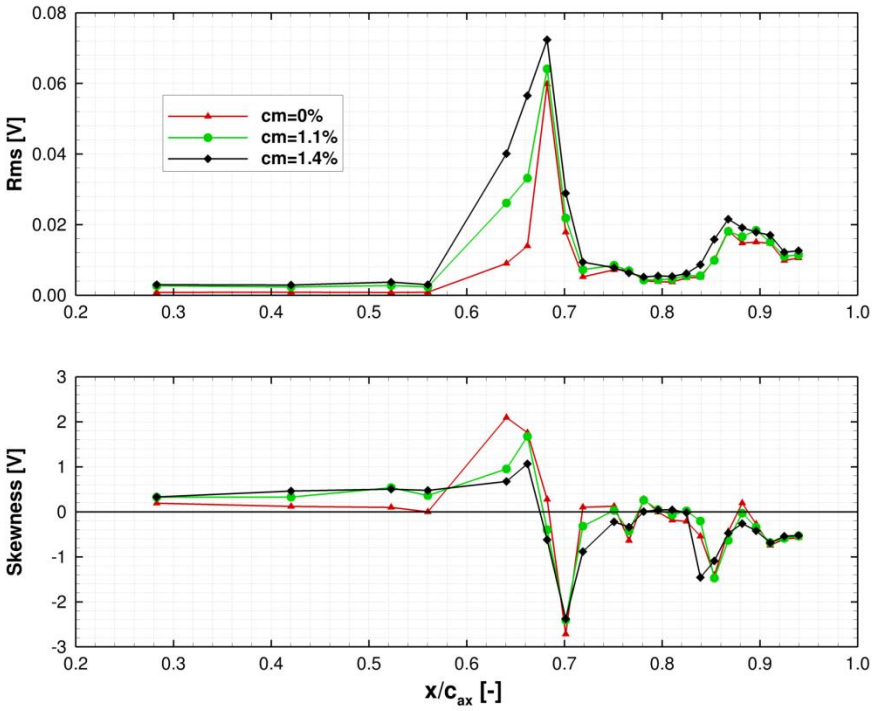

Figure 24 Rms and Skewness of fluctuating hot-film voltages

A peak of the Rms data is found for all three cases at the same position. At that position the intermittency is approximately at 50 percent (Howell2002). The skewness data show an inflection point after reaching a positive peak. Further downstream the boundary layer starts to become turbulent with the negative peak of the skewness data. The normal shock at $x/c_{ax} \approx 0.9$ increases the boundary layer thickness. This is indicated by the rise in Rms data and the second negative peak of skewness.

The comparison of three different coolant mass flow ratios shows initially higher positive skewness and higher Rms values for the cases with coolant flow. Howell2002 declares this state as a predominantly laminar boundary layer with occasional turbulent components. The beginning of separation at $x/c_{ax} \approx 0.6$ (Figure 22) shows remarkable higher Rms data with higher coolant mass flow ratio. This is clearly shown for the fluctuating voltages, as well (Figure 23).

The next Figure 25 shows the Amplitude spectra for voltages at alternating current of all three coolant mass flow ratios. The recorded data have an amount of 65536 samples at a sample frequency of 64000. Considering the Nyquist criteria while applying the FFT are shown frequencies up to 32 kHz.

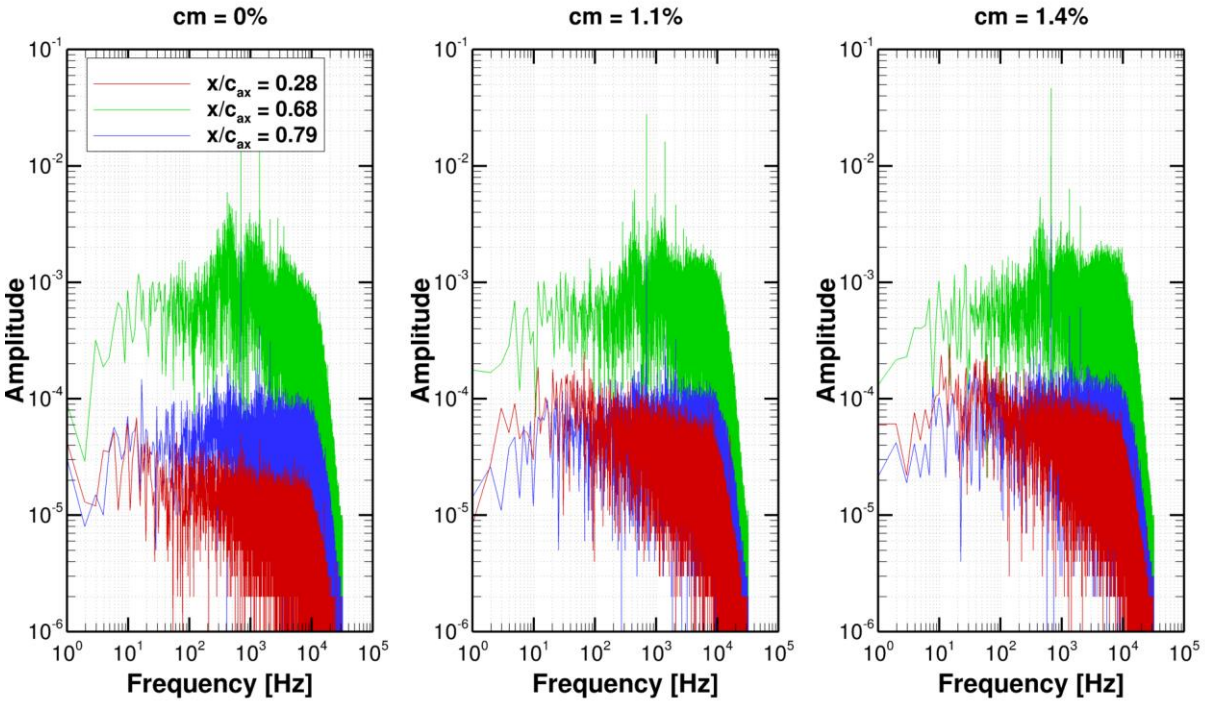

Figure 25 Amplitude spectra of fluctuating hot-film voltages

For this figure were three wires chosen. Primarily is the first wire at $x/c_{ax} \approx 0.28$ is shown in red. The transitional region at 50 percent intermittency at $x/c_{ax} \approx 0.68$ has high amplitudes. These effects were already described in Johnson1989. Additionally, the third spectra at $x/c_{ax} \approx 0.79$ show the turbulent boundary layer at all coolant mass flow ratios. The amplitudes at $x/c_{ax} \approx 0.28$ are lower than for the turbulent regions. Remarkably lower are these at no coolant flow. The holes itself do not induce the change of boundary layer state. For the cases with coolant flow the disturbances increase the turbulent level. A definition of this boundary layer state cannot be completed with the given data.

8. Comparison of blade surface measurements

In this chapter all measurement techniques applied on the blade surface will be compared. The data shown in Figure 26 are Mach number distribution, infrared data and hot-film data over the relative x-positions. The distorted profile geometry with the hot-film wire positions is shown as well.

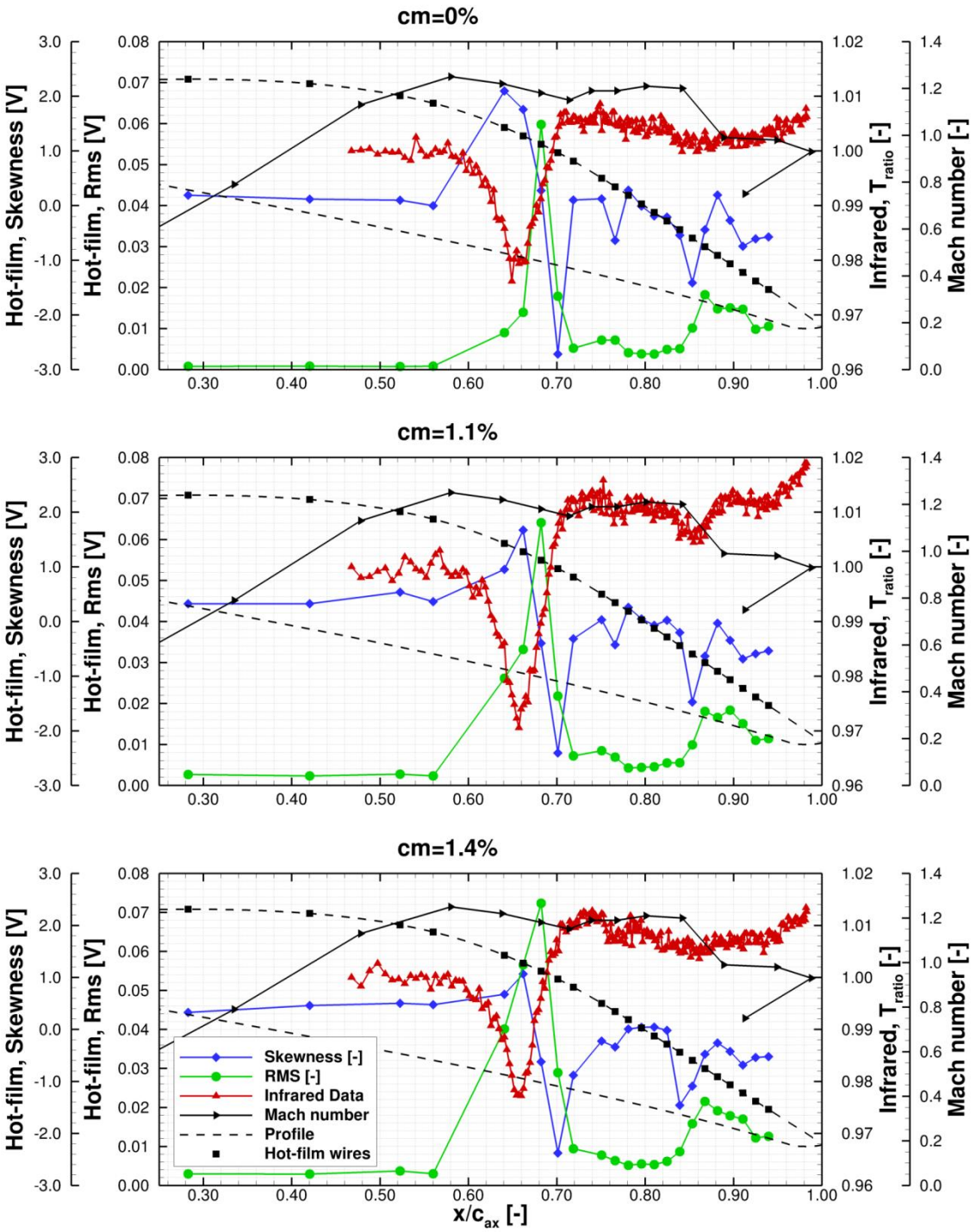

Figure 26 Comparison of temperature distribution, hot-film statistical data and Mach number distribution

The incidence shock induces a separation. This is revealed by the temperature ratio of the infrared measurement. The peak of the Rms value is located at the highest growth of the temperature ratio after its minimum at $x/c_{ax} \approx 0.68$. This indicates a separation induced transition. This effect can be found for all three coolant mass flow ratios. Hence, the transition process changed with introduction of coolant flow. Where at the basic case the laminar boundary layer partial survives the incidence shock at the passage does this clearly not happen for the coolant flow cases.

Summary

At transonic flow conditions experimental research was carried out at high pressure turbine stator blades in a straight cascade to determine the aerodynamic behavior. Special emphasis is laid on detection of the transition location. Its influence on the shock wave boundary layer interaction is the main research issue at the TFAST project. The main investigation assessment for a turbine is the aerodynamic loss. In this work package is put a special stress to this criteria. Two cascade set-ups were applied, one without coolant and the other with coolant flow. The experiments were performed at the Wind Tunnel for Straight Cascades at the German Aerospace Centre, Göttingen. The profile geometry was designed by RollsRoyce Deutschland (RRD) to sustain high loads and for relaminarization of the boundary layer.

The inlet parameters 80 mm upstream of the blade leading edge were investigated with a hot-wire anemometer and a pressure probe. These data were measured to provide inlet conditions for their work to the partners with numerical tasks. One of the solid blades without coolant ejection was equipped with pressure taps to obtain the surface pressure distribution. Further information about the flow field was obtained by the application of Schlieren technique and wake traverse measurements. The transition location was detected with an infrared camera and a stripe of 28 hot-film elements on the suction side of a cooled blade. All measurements were performed at zero incidence angle and the transonic exit Mach number ≈ 1.05. The inlet pressure was given at 115 kPa and the inlet temperature at 300 K. As there is no emphasis laid on coolant efficiency, but transition location and aerodynamic performance, the temperature of the coolant flow is set to inlet temperature. The Reynolds number is in the range of $Re \approx$ 1.1 Mio.

At application of the cooled cascade three blades were equipped with coolant cavities. Each cavity had two coolant rows. One exits at the stagnation point and the second one in the acceleration region on the suction side. Measurements of the cooled cascade without coolant flow were undertaken to investigate the influence of the holes itself on the transition location. Besides, RRD specified the coolant pressure to 120.7 kPa, which gives a coolant mass flow ratio of 1.1%. Additionally, a higher coolant mass flow of 1.4 % was applied to investigate the coolant flow influence on the transition location.

Subsequently the specific research findings of this investigation are summarized:

Shock structure

The incidence shock at the passage causes separation at all measured cases. This indicates the reflected expansion wave and a separation as well as a reattachment shock. Downstream of the passage appears a normal shock at $x/c_{ax} \approx 0.85$. This shock terminates the reflections of the upstream shock system. At the trailing edge emerges a second weaker normal shock. A comparison of different pictures at each case revealed unsteadiness effects. The strong normal shock oscillated with the highest amount of amplitudes.

Separation

The obtained temperature distribution by the infrared camera revealed a separation bubble caused by the incidence shock in the passage. The introduction of coolant flow shifted the separation onset 2% of relative axial chord downstream. A significant shortening of the separation bubble could not be achieved.

Transition location

At the basic blade without coolant flow the incidence shock at the passage induced a partial transition of the boundary layer state. Nevertheless, this did not happen for the whole

boundary layer. The observed temperature distribution revealed turbulent wedges. These could not be observed at the cooled blade. At the cooled blade a separation induced transition could be observed at all three different mass flow rates. Additionally, a thickening of the boundary layer due to the strong normal shock is found.

Turbine loss coefficient

Applied was the aerodynamic loss coefficient which does not include coolant mass flow. The losses decrease with the increase of coolant mass flow by approximately 0.15%. Meanwhile, the downstream Mach number measured by a probe increases at the cooling blade with increase of coolant mass flow.

References

Acronym	*Reference*
Amecke1995	Amecke, J.; Safarik, P.: *Data Reduction of Wake Flow Measurements with Injection of an Other Gas.* DLR-FB 95-32, 1995.
Babinsky2011	Babinsky, H.; Harvey, J. K.: *Shock Wave-Boundary-Layer Interactions.* Cambridge University Press, 2011.
Burd1999	Burd, S.W.; Simon, T.W.: *Measurements of Discharge Coefficients in Film Cooling*. Journal of Turbomachinery, 121, 243-248, 1999.
Howell2002	Howell, R. J. et al: *Boundary Layer Development in the BR710 and BR715 LP Turbines—The Implementation of High-Lift and Ultra-High-Lift Concepts.* Journal of Turbomachinery, 124, 385-392, 2002.
Johnson1989	Johnson, C.; Carraway, D.: *A transition detection study at Mach 1.5, 2.0 and 2.5 using a micro-thin hot-film system*. Instrumentation in Aerospace Simulation Facilities, 1989. ICIASF '89 Record., International Congress on, 82-94, 1989.
Fey2006	Fey, U.; Egami, Y. & Engler, R.: *High Reynolds Number Transition Detection by Means of Temperature Sensitive Paint.* Aerospace Sciences Meetings, American Institute of Aeronautics and Astronautics, 2006.
Jung2001	Jung, K.: *Mehrreihige Filmkühlung an gekrümmten Oberflächen*. Dissertation, TU Darmstadt, 2001.
Kiock1985	Kiock, R. et al.: *The boundary layer behaviour of an advanced gas turbine rotor blade under the influence of simulated film cooling*. AGARD Heat Transfer and Cooling in Gas Turbines 19, 1985.
Kost2004	Kost, F.; Giess, P. A.: *Experimental Turbine Research at DLR Göttingen*. Journal of the Gas Turbine Society of Japan, Volume 32(6), Pages 485-493, 2004.
Kost2009	Kost, F.: *THE BEHAVIOR OF PROBES IN TRANSONIC FLOWFLIEDS OF TURBOMACHINERY*. European Conference on Turbomachinery, Volume 8, 2009.
Lutum1999	Lutum, E.; Johnson, B. V.: *Influence of the Hole Length-to-Diameter Ratio of Film Cooling With Cylindrical Holes*. Journal of Turbomachinery, 121, 209-216, 1999.
Nikon2000	Nikon Corporation: *Laird-S270A, Operation Manual.* Japan, May 2000.
Ren2010	Ren, C.: *Calibration of a four-hole mini-probe in sub-, trans- and supersonic flow.* DLR-IB 225-2010 A08, 2010.
Shapiro1953	Shapiro, A.H.: *Compressible Fluid Flow.* Volume1. The Ronald Press Company, New York, 1953.
Zwillinger2000	Zwillinger, D.; Kokoska, S.: *CRC Standard Probability and Statistics Tables and Formulae*. Chapman & Hall: New York. 2000.

Symbols

A	**area**
A/D	**Analog to digital**
AJVG	**Air jet vortex generator**
c	**chord**
CJC	**Co-Juction-Compensation**
c_m	**coolant mass flow ratio**
DLR	**German Aerospace Center**
F	**Frequency**
FFT	**Fast Fourier transform**
h	**width on blade**
K	**NiCr NiAl**
$\dot{m}$	**mass flow**
Ma	**Mach number**
N, n	**quantity**
p	**pressure, probe hole**
PSD	**power spectra**
PSI	**Pressure Systems**
R	**specific gas constant**
Rms	**Root mean square**
RRD	**RollsRoyce Deutschland**
ST	**skew terminal**
t	**time, pitch**
T	**temperature**
Tu	**turbulence intensity**
u	**velocity**
U	**voltage**
u'	**fluctuating velocity**

U’	fluctuating voltage
x	length in flow direction
y	length in spanwise direction

Greek Symbols

α	circumferential angle
β	radial angle
κ	Heat capacity ratio
ξ	loss coefficient
τ	time difference

Indices

01	total condition at inlet
02	total condition at outlet
0s	centre (probe hole)
2	static condition at outlet
ax	axial
c	coolant
EGG	Wind tunnel for Straight cascades
h	channel width
i	quantity
S	aerodynamic
sr	right (probe hole)
std	standard variance
wo	upper (probe hole)
wu	lower (probe hole)
y	probe, length in spanwise direction

List of Figures

List of Tables

Appendix

Table 4 Positions of pressure taps on blade contour

Nr.	c_{ax} *[%]*	c_y*[%]*	*Nr.*	c_{ax} *[%]*	c_y*[%]*
1	**18,26**	**24,21**	11	**68,21**	**10,03**
2	**9,11**	**15,63**	12	**71,35**	**16,96**
3	**2,05**	**5,77**	13	**73,92**	**23,58**
4	**0,49**	**-3,40**	14	**76,83**	**31,43**
5	**5,10**	**-11,87**	15	**80,15**	**40,81**
6	**17,45**	**-19,76**	16	**84,16**	**52,46**
7	**33,51**	**-21,41**	17	**88,94**	**66,51**
8	**47,85**	**-16,75**	18	**94,89**	**83,70**
9	**58,00**	**-7,59**	19	**98,78**	**99,95**
10	**63,77**	**1,38**	20	**91,28**	**92,37**